Fast and localized temperature measurements during simulated earthquakes in carbonate rocks

Stefano Aretusini[1], Arántzazu Núñez-Cascajero[2], Elena Spagnuolo[1], Alberto Tapetado[2], Carmen Vázquez[2], and Giulio Di Toro[1,3]

[1]Istituto Nazionale di Geofisica e Vulcanologia, Roma, Italy.

[2]Universidad Carlos III de Madrid, Electronic Technology Department, Leganés, Spain.

[3]Università degli Studi di Padova, Department of Geosciences, Padova, Italy.

Corresponding author: Stefano Aretusini (stefano.aretusini@ingv.it)

Key Points:

- Optical fibers were used to measure temperature evolution during simulated seismic slip
- Temperatures were up to 1250 °C and compatible with coseismic grain size dependent creep.
- "Frictional work" during simulated seismic slip was mostly dissipated as heat.

Key words

earthquake, optical fiber, laboratory experiments, temperature measurement, viscous creep

Abstract

The understanding of earthquake physics is hindered by the poor knowledge of fault strength and temperature evolution during seismic slip. Experiments reproducing seismic velocity (~1 m/s) allow us to measure both the evolution of fault strength and the associated temperature increase due to frictional heating. However, temperature measurements were performed with techniques having insufficient spatial and temporal resolution. Here we conduct high velocity friction experiments on Carrara marble rock samples sheared at 20 MPa normal stress, velocity of 0.3 and 6 m/s, and 20 m of total displacement. We measured the temperature evolution of the fault surface at the acquisition rate of 1 kHz and over a spatial resolution of ~40 µm with an optical fiber conveying the infrared radiation to a two-color pyrometer. Temperatures up to 1250 °C and low coseismic fault shear strength are compatible with the activation of grain size dependent viscous creep.

1 Introduction

During earthquakes, energy is radiated as elastic waves because of the imbalance between the elastic strain energy released around a fault and the energy dissipated within the fault (Scholz, 2019). This happens because fault rocks lose strength faster than the stress drop around the fault (Nielsen et al., 2016). Laboratory experiments can reproduce both the evolution of the shear strength on a point of a fault (Tsutsumi & Shimamoto, 1997) and the nucleation and propagation of the seismic rupture (Ohnaka & Shen, 1999) on temporal and spatial scale to provide insight on the deformation processes controlling earthquake mechanics.

During earthquakes, fast sliding (up to 10 m/s) along faults and dissipation of the mechanical energy over short times increases the heat rate production. Temperature increases because the frictional heat dissipated in the fault slip zone is higher than the heat conducted away from the rocks bounding the fault (McKenzie & Brune, 1972). Heat conduction is inefficient because the rocks have low thermal diffusivity which further decreases with increasing temperature (Merriman et al., 2018; Miao et al., 2014). As the temperature on the fault surface increases with slip, the fault strength decreases (i.e., dynamic weakening) due to thermally-activated deformation mechanisms, phase changes and chemical reactions (Rice, 2006; Di Toro et al., 2011). For example, in silicate-built rocks commonly found at shallow–to-intermediate crustal depth (granite, gabbro, basalt, etc.), frictional melting of most minerals (feldspars, biotite, etc.) occurs in the fault slip zone, as attested by the presence of solidified friction-induced melts (i.e., "pseudotachylytes", Sibson, 1975). In addition to silicate-built rocks, carbonate rocks can also host earthquakes at shallow crustal depth (e.g., the 2008 Wenchuan earthquake, see Chen et al., (2013); or the 2009 and 2016 earthquake sequences in the Appenninnes, see Demurtas et al., (2016)). In room-dry carbonate rocks, dynamic weakening has been ascribed to amorphization of calcite mineral (Spagnuolo et al., 2015) and thermal decomposition of calcite into lime (Han et al., 2007). Moreover, low dynamic shear strength was proposed to be driven by crystal plastic deformation processes and in particular by grain size sensitive viscous creep (Ashby & Verrall, 1973; Schmid et al., 1977), facilitated by the presence of nanometric particles (Demurtas et al., 2016, 2019; Green et al., 2015; Ohl et al., 2020; De Paola et al., 2015; Pozzi et al., 2019). All the aforementioned dynamic weakening processes depend on the rock's mineral composition and on the magnitude of the temperature increase. Therefore, the temperature evolution with seismic slip is the most relevant parameter governing dynamic weakening and earthquake rupture propagation.

At the early stage of seismic slip, individual micrometer-sized asperity contacts constitute the real contact area supporting the normal stress on the fault (Scholz & Engelder, 1976). Since the real contact area is smaller than the total fault surface, the shear stress and the frictional power per unit area (i.e., product of shear stress per velocity, Di Toro et al., 2011) dissipated on the asperities are larger than the average stress and frictional power on the total fault surface. Therefore, the temperature rise is fast and localized on the asperity contacts as proposed in the "flash heating" theory (Archard, 1959; Beeler et al., 2008; Rice, 2006). Hot spots ~10 µm in diameter are supporting the normal stress, deforming and weakening while heating up to hundreds of degrees in 10^{-6}-10^{-5} s (Beeler et al., 2008).

So far, no experimental technique was effective in measuring the temperature directly or approaching the asperity contacts scale. In fact, thermocouples can measure temperature directly on the fault surface but have a large inertia compared to the timescale of the earthquake processes (10^{-6}-10^{-5} s) as the electric potential developing in response to the temperature gradient happens in ~0.1 s and is limited by heat conduction (Sarnes & Schrüfer, 2007). For these reasons, thermocouples are not suitable to measure the ultra-fast and localized temperature increase at the asperity scale. Infrared rays (IR) are produced from the temperature increase on surface contacts and can be sampled with IR cameras. IR cameras have a spatial resolution of 0.3 mm, insufficient to resolve spatially the asperity contacts. However, with additional close-up lens, resolution can increase up to 70 µm (Barbery et al., 2019), but the measurements record the temperature outside of the slipping zone and are affected by the air turbulence around the sample. Acquisition times of 0.02 s are common but can be decreased to ~$3 \cdot 10^{-5}$ s using special digitalization processes (Usamentiaga et al., 2014). Moreover, the emissivity of the deforming material has to be measured to calibrate the absolute temperature from the IR images (Núñez-Cascajero et al., 2020).

In this study we present the first measurements of slip zone *in-situ* temperature collected with high spatial and time resolution and recorded during experiments simulating seismic slip. With the rotary machine SHIVA, we sheared Carrara marble experimental faults at seismic velocity to simulate earthquake propagation on carbonate fault rocks. We measured simultaneously: i) the shear strength and ii) the temperature on the sheared fault by sampling the IR radiated from the slip zone with a two-color fiber-optic pyrometer. The location of the fiber on the slip surface, coupled with the high spatial (37 µm) and temporal (0.001 s) acquisition of the pyrometer, allowed us to directly measure the temperature *inside* the slip zone. The measured temperature during coseismic slip was up to 1250°C, 300-400°C higher than the one estimated previously with IR cameras, thermocouples, and numerical models. These *in-situ* temperature measurements are consistent with the activation of calcite thermal decomposition and of grain size dependent viscous creep, which govern the measured large dynamic fault weakening and the *on-fault* energy budget of the simulated earthquake.

2 Methods

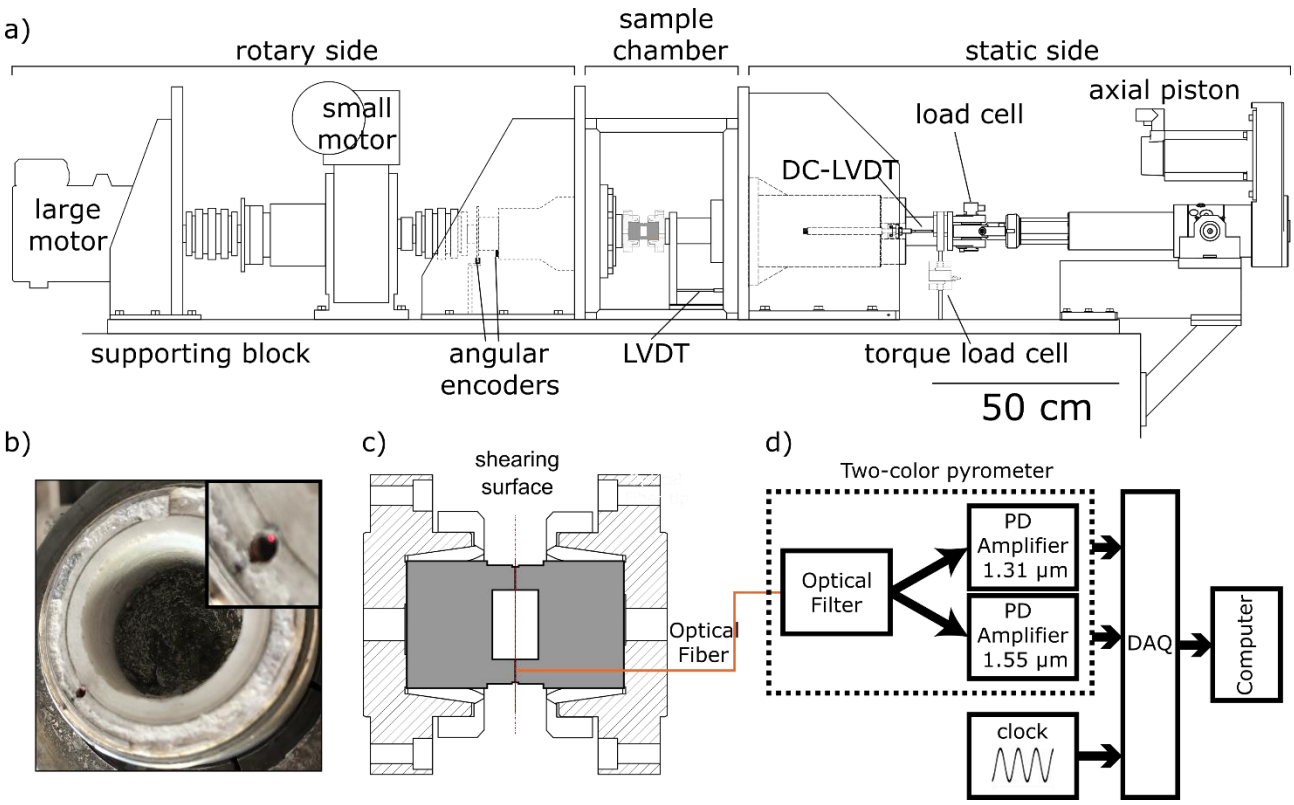

Figure 1. Experimental setup. a) SHIVA apparatus (Section 2.2). b) Top view of the shearing surface on the rock sample after one experiment. In the inset, the optical fiber tip (red spot) is emitting light. This preliminary test for fiber integrity was performed connecting the optical fiber to an LED before and after each experiment. c) Cross section of the sample chamber: two hollow rock samples are indicated in grey. d) Two-color pyrometer measurement setup connected to the fiber collecting IR from the rock sample surface.

2.1 Sample preparation

The rock samples tested in the experiments were made of Carrara marble (ca. 99 wt.% calcite, 1 wt.% quartz). The samples were two hollow cylinders with 15/25 mm internal/external radiuses and 50 mm height. The bases of the hollow cylinders in contact during the experiments were worked with a lathe to obtain surface contact parallelism when installed in SHIVA (Nielsen et al., 2012). This lathe treatment produced a ~#2000 roughness on the surface, corresponding to an asperity diameter of ca. 10 µm (Cornelio et al., 2019; Spagnuolo et al., 2015). On the contact surface between the two hollow cylinders an optical fiber end was placed by means of a hole (1-

123 1.2 mm diameter) drilled parallel to the cylinder axis, at a distance of 20.2 mm from the center of
124 the sample. The fiber was glued to the lateral sides of the hole using a heat-resistant silicate glue,
125 stable up to 1200 °C (Everbuild). Before and after each experiment, the fiber was connected to an
126 LED to test for integrity and capability to transmit light (Fig. 1b).
127
128 **2.2 High velocity friction experiments**
129 The high velocity friction (HVF) experiments were performed in the Slow to High Velocity
130 Apparatus (SHIVA) (Di Toro et al., 2010) (Fig. 1a). SHIVA is constituted of a rotational shaft
131 connected to two electric motors and an axial shaft connected to an electromechanical piston.
132 Samples are deformed in the central sample chamber. On the axial side, the normal force is
133 measured with a load cell in line with the sample axis and the torque on the axial column with an
134 S-beam load cell attached to an arm fixed to the frame of the apparatus. Normal stress was
135 calculated by dividing the normal force by the nominal sample contact area (i.e., 0.0013 m^2) and
136 torque was converted to shear strength following Shimamoto & Tsutsumi (1994). The
137 displacement normal to rock contact surface was measured with an LVDT (1 μm resolution). The
138 measurement of axial displacement was used to monitor the rock sample dilatancy/shortening
139 during the experiments. The rotation of the rotary shaft was imposed with an electric motor,
140 capable to impose angular velocities up to 3000 rpm. By combining two encoders measurements
141 we obtained the incremental displacement and, using numerical derivation with respect to time,
142 velocity. Both displacement and velocity are referred to the radial position r=20.2 mm where the
143 optical fiber was located. The measurements of normal force, torque, axial displacement, and
144 incremental rotation were at up to 12500 Hz. An analog clock signal produced with a function
145 generator was acquired to synchronize the temperature and the high velocity friction
146 experimental measurements. The experiment consisted in stepwise increase of the normal stress

147 up to 20 MPa. Then the samples were sheared imposing a trapezoidal velocity function with an
148 acceleration, equal to the final deceleration, of 6.8 m/s^2 to the target velocity *V* of 0.3 or 6 m/s for
149 a total displacement *d* of 20 m.
150
151 **2.3 Two-color pyrometer**
152 The pyrometer setup uses the same topology of a previous study (Fig. 1c, Tapetado et al.,
153 2016) with the main difference of using a single mode fiber (SMF), low-noise photodetectors, and
154 a dedicated filter (Núñez-Cascajero et al., 2020). The SMF has core and cladding diameter of 9 and
155 125 µm, respectively, and a numerical aperture of 0.14. A low insertion loss WDM filter spatially
156 splits the radiation collected by the optical fiber into two spectral bands centered at 1.31 and 1.55
157 µm, respectively. Two InGaAs photodetectors with uniform responsivity at both wavelength bands
158 and transimpedance amplifiers were used to convert the radiant flux into a voltage signal. Before
159 each acquisition, the gain of the amplifier and the range of the voltage signals were set to avoid
160 that the amplified signal exceeded the output range. The measurements of the radiant flux from
161 the photodetectors in the two spectral bands and of the analog clock signal obtained with the
162 function generator were acquired at 1 kHz. The two-color pyrometer measurements were
163 synchronized with the measurements during the HVF experiments by minimizing the time delay
164 between the clock signals recorded with the separate acquisition systems. The relationship
165 between radiant flux I_D (V) and temperature *T* (°C) was obtained in a calibration test. This test was
166 done in a dry block calibrator with a blackbody kit, in the range from 250 to 1100 °C, to account
167 for all the instrumental contributions of the measurement system (Núñez-Cascajero et al., 2020).
168 The radiant fluxes measured during the HVF experiments, $I_{D,1.3}$ and $I_{D,1.5}$, (corresponding to
169 the two spectral bands centered at 1.31 and 1.55 µm) were converted to single channel
170 temperatures ($T_{1.3}$ and $T_{1.5}$) using the relation obtained in the calibration tests and assuming that

171 the surface emissivity was the same both in the calibrator and during the experiment ($\varepsilon_c/\varepsilon$ = 1, Eq.
172 S6).
173
174 **2.4 Emissivity of Carrara marble**
175 To obtain Carrara marble rock emissivity and compute the relative temperature error, a
176 separate calibration was performed. We prepared a disk of Carrara marble rock with: 15 mm
177 external radius, 4 mm thickness, and a central hole with a 3 mm diameter. The bases of the
178 cylinder were roughened with #2000 sandpaper to apply a roughness equivalent to the one of the
179 contact surface of rock samples used in the experiments. The disk was placed into a dry block
180 calibrator. The control unit of the dry block calibrator furnace ensures a maximum temperature
181 stability and uncertainty of ±0.03 and ±0.17 °C, respectively, in the range from 50 to 650 °C. The
182 radiant flux emitted by the rock disk surface was characterized in the 1.31 and 1.55 µm spectral
183 bands ($I_{D,1.3}$ and $I_{D,1.5}$), while temperature was stepped from 300 up to 650 °C. Measurements
184 were made every temperature step of 25 °C, waiting for 45 min to stabilize temperature at each
185 step. The sampling rate and the number of samples at each temperature and wavelength were
186 fixed at 1 kHz and 500 samples, respectively.
187
188 **3 Results**
189
190 **3.1 High velocity friction and temperature measurements**
191 Shear strength of the slip zone (τ), divided by the applied normal stress (S_n) was converted
192 into the apparent friction coefficient $\mu=\tau/S_n$. During the first 0.5 m of slip, the apparent friction
193 achieved a peak value μ_p = 0.54±0.13 independently of the target velocity and then decayed

194 towards a residual value (μ_r) which decreased with increasing velocity (i.e., ca. 0.14 at 0.3 m/s and
195 ca. 0.06 at 6 m/s, respectively, Fig. 2).

196 Herein, we present the mean ± standard deviation of temperature in all measurement
197 channels. In the experiments performed at 0.3 m/s (s1680 & s1682), temperature $T_{1.5}$ at μ_p was
198 467±99 °C, and then increased monotonically up to a constant value of 1077±37 °C at the μ_r for
199 large slip values (17.8<d<20 m). In the experiments performed at 6 m/s (s1684 & s1686),
200 temperature $T_{1.5}$ at μ_p was 684±108 °C, and then increased up to 1248 °C after μ_r was achieved for
201 2.2<d<6.6 m. After this maximum value, $T_{1.5}$ decreased to 1136±90 °C after 17 m of slip (i.e.,
202 before the onset of the deceleration stage and the end of slip).

203 In the experiments at 0.3 m/s, the sample shortened of 0.39-0.54 mm (mostly at d>5 m). At
204 6 m/s, sample shortening was negligible (0.007-0.061 mm), occurred at slip initiation (d<0.5 m)
205 and no drops in temperature were detected. Previous studies demonstrated that the temperature
206 measurements are independent from the damage of the fiber tip except when damage resulted in
207 occlusion of the fiber tip (Tapetado et al., 2017). Partial occlusion by production of wear particles
208 could explain the temperature drops observed in experiment s1680 at ca. 17.8 m of slip.
209

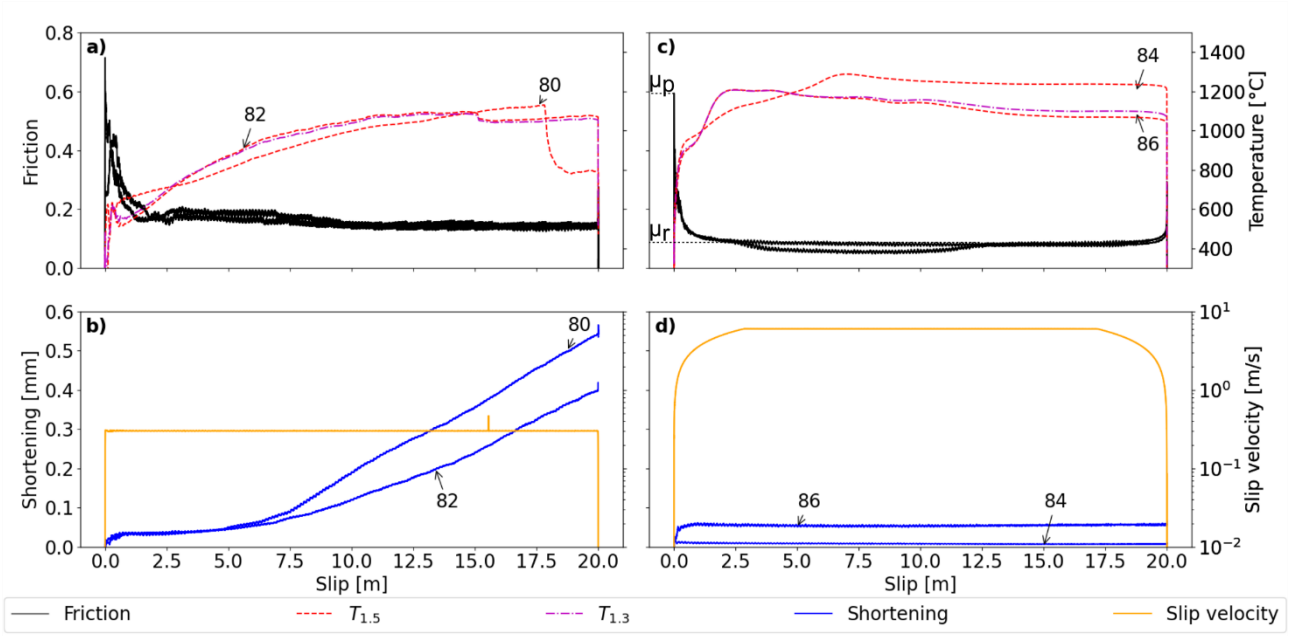

Figure 2. Experimental results. Measurements of temperature $T_{1.5}$ and $T_{1.3}$, friction coefficient, shortening and velocity vs. slip. Panels a)-b) contain experiments s1680 and s1682, performed at V=0.3 m/s. Panels c)-d) contain experiments s1684 and s1686, performed at V=6 m/s. All the presented data are available in an open access repository (Aretusini et al., 2020).

4. Discussion

4.1 Spatial resolution of the temperature measurement

Previous studies showed that the spatial resolution of temperature measurement with the pyrometer technique depending on the distance between the fiber tip and the target surface and on the numerical aperture of the fiber (Núñez-Cascajero et al., 2020). The spatial resolution can be calculated from the projected diameter of the fiber core on the heated surface as:

$$D_{NA} = 2t \cdot tan(arcsin(NA)) \quad (1)$$

where *NA* is the numerical aperture of the optical fiber and *t* the distance between the fiber tip and the heated surface. Considering our SMF fiber, with a numerical aperture of 0.14, and a fiber tip to surface distance of 100 µm, we calculated that D_{NA} was of 37 µm.

The slip surface topography consists of more or less regularly spaced (ca. 50-100 µm apart) troughs and ridges parallel to slip direction (Spagnuolo et al., 2015; Tisato et al., 2012) (see Fig. S1). Therefore, the spatial resolution of the temperature measurement is less or equal to the maximum width of the ridges. On the other hand, the irregular topography of the fault surface might result in projecting the fiber's tip onto the trough areas between the ridges, resulting in a temperature measurement lower than the one achieved at the ridges. As a consequence, the temperature measured from the heated surface is averaged over a small circle with diameter of ca. 37 µm considering a fiber-to-surface distance of 100 µm (Eq. 1). This makes the temperature information localized in space, but possibly still up to five times larger than the diameter of the average rock asperity before sliding ensues (i.e., 7 µm in marbles with identical sample preparation procedure, Cornelio et al., (2019)). In conclusion, the measured temperature is not related to a single asperity or ridge, but it is probably the temperature resulting from the contribution of several hot asperities and colder troughs. For this reason, albeit localized, the measured temperature is still an average surface temperature and flash temperatures were not detected, also because of the low acquisition rate (1 kHz, while to measure flash temperatures acquisition rates should be increased to 1 MHz). Considering the sampling time of 0.001 s and the velocity of 0.3 and 6 m/s, the measured temperature was from an area elongated along slip direction of ca. 0.3 and 6 mm, respectively.

4.2 Temperature relative error of $T_{1.3}$ and $T_{1.5}$

248 The error between the “real” temperature of the sliding surface and the estimated
249 monochromatic temperature increases with (Eqs. S6, S7): i) the bulk temperature of the surface, ii)
250 the ratio between the emissivity of the calibration surface and of the deforming surface, and iii)
251 the wavelength of the channel. The measured emissivity of Carrara marble in the 425-650 °C range
252 varied between 0.93 and 1 (Fig. S2a), and was very similar to the calibration surface (a blackbody
253 with emissivity of 0.99). Because of this, the relative error was below 0.5% in both $T_{1.3}$ and $T_{1.5}$ at
254 600 °C (Fig. S2b). Assuming that in the 650-1300 °C range emissivity of Carrara marble decreased
255 to 0.8 (e.g. because of the calcite thermal decomposition), temperature errors would be in the
256 order of 1.25% ($T_{1.3}$) to 1.5% ($T_{1.5}$) at 650 °C and 2.5% ($T_{1.3}$) to 3% ($T_{1.5}$) at 1500 °C (Fig. S2b).
257
258 **4.3 Implications for dynamic weakening processes in simulated earthquakes**
259 The measured temperature increase in the slip zone is compatible with the activation of
260 chemical reactions and deformation mechanisms as proposed in theoretical studies (Sulem &
261 Famin, 2009), supported by experimental evidence of release of CO_2 during sliding (Spagnuolo et
262 al., 2015), and by evidence of decarbonation products in post-mortem samples (Han et al., 2007;
263 Mitchell et al., 2015; Violay et al., 2013, 2014, 2015). Moreover, the strong inverse dependence of
264 fault shear strength with velocity support the hypothesis that the measured “dynamic weakening”
265 is correlated to the temperature increase by frictional heating during simulated earthquake slip (Di
266 Toro et al., 2011).
267

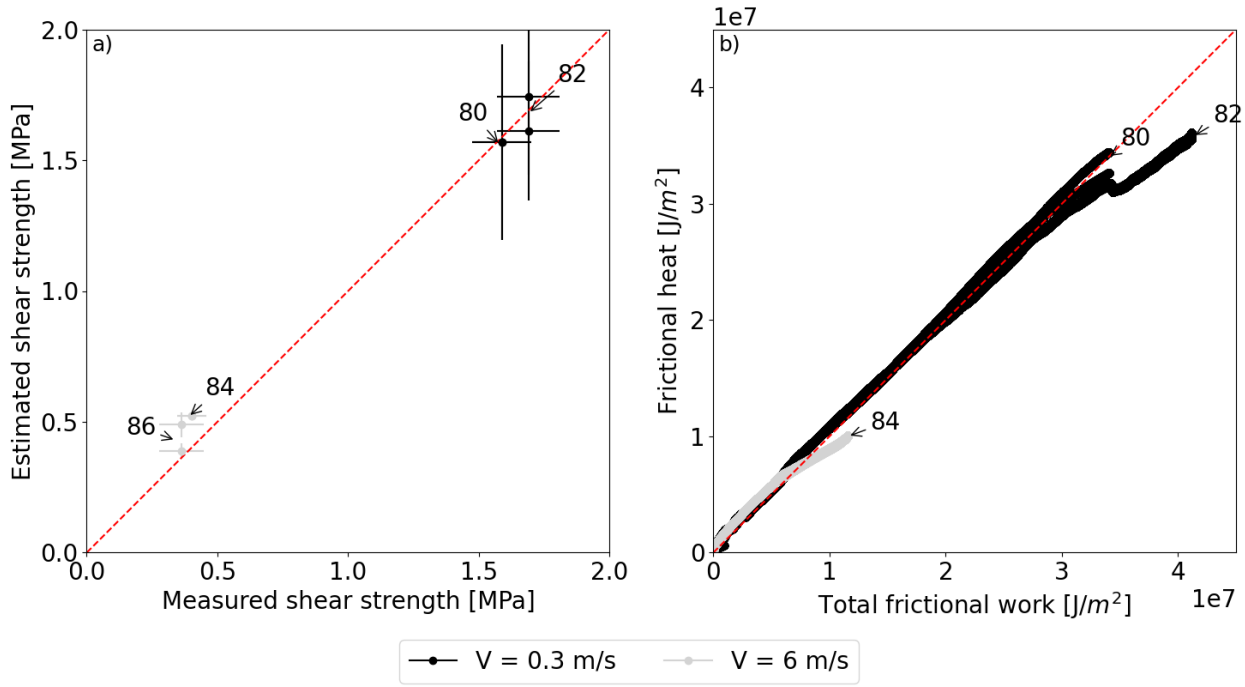

Figure 3. a) Measured shear strength versus the shear stress estimated by GBS. GBS predicts shear strength values similar to the experimental ones at large slip (12 < d < 17 m), when temperature exceeds 1000 °C. See section 4.3 for discussion. b) Energy dissipation on the fault surface. The total frictional work calculated from the measurements of shear strength and velocity (x-axis) is compared against the frictional heat calculated from the temperature measurement (y-axis). See section 4.4 for discussion. The final part of experiment s1680 was removed due to partial occlusion of the optical fiber.

Thermal decomposition of calcite into lime and CO_2 is usually starting at ca. 600 °C, in CO_2-poor atmosphere (Rodriguez-Navarro et al., 2009) and at 900 °C in CO_2-rich atmosphere at 0.1 MPa (Criado et al., 1995). These decomposition temperatures are easily overcome at slip initiation, either at peak friction for target V=6 m/s (Figure 2c) or in the first 2 meters of slip for target V=0.3 m/s (Figure 2a). Thermal decomposition and wear were proposed to produce a slip zone with a finite thickness on top of the asperity "ridges" (Fig. S1), in which particles of <100 nm in size are found ("nanoparticles", Han et al., (2007), Figure S1). Nanoparticles can promote grain-

size dependent viscous creep as grain boundary sliding (hereafter GBS; Schmid et al., (1977)). Especially at the high temperatures (i.e., > 600-900 °C) and strain rates (~10^4 1/s) characteristic of seismic slip, GBS can determine a very low fault shear strength and therefore promote dynamic weakening as evidenced by the absence of crystal preferred orientation (Demurtas et al., 2019; De Paola et al., 2015; Pozzi et al., 2018, 2019).

Since our temperature measurements are localized, they resulted 300-400 °C higher than those measured or estimated in previous studies (1250°C vs. 900°C in Han et al., 2007) and higher than the theoretical temperature of decarbonation, which would limit the maximum temperature in the slip zone to ca. 900 °C because this endothermic reaction would buffer the temperature increase (Sulem & Famin, 2009). The low porosity of the thin layer made of nanoparticles (Pozzi et al., 2019) may promote a pore pressure increase so that, because of the equilibrium between $CaCO_3$ and CO_2, higher temperatures are required to have decarbonation of calcite (Criado et al., 1995). Assuming decarbonation occurs under equilibrium conditions, the maximum pore pressure calculated from temperature reduces the effective normal stress so that, given a friction coefficient of 0.6 (Rempe et al., 2020), the bulk shear strength decrease may account for 8% (i.e., at 0.3 m/s) and 16.7-32.8% (i.e., at 6 m/s) of the total dynamic strength drop measured in the experiments. However, both pristine and decarbonated Carrara marble rocks can achieve similar dynamic weakening, suggesting that the thermally-activated deformation processes acting in nanoparticle layers dominate over the pressure-dependent processes (Han et al., 2007; De Paola et al., 2011).

The shear strength of a deforming zone according to GBS is (Schmid et al., 1987):

$$\tau = \left(\frac{\dot{\gamma} \phi^{b}}{\left(\sqrt{3}\right)^{n-1} A \exp\left(-\frac{E_a}{RT}\right)} \right)^{1/n} \quad (2)$$

305

306 with the shear strain rate $\dot{\gamma}$ (1/s) expressed as the ratio V/h, between the velocity V (m/s) and the
307 thickness of the deforming zone h (m), the grain size ϕ (m) and the grain size exponent b, the pre-
308 exponential term A ($s^{-1}bar^{-n}\mu m^{b}$), the activation energy E_a (kJ/mol), the ideal gas constant R
309 (0.00831 kJ/(mol·K)), the temperature T (K), and the stress exponent n. GBS process in fine grained
310 carbonates was described by: stress exponent n = 1.66, grain size exponent b = 3, pre-exponential
311 $A=10^{4.98}$ ($s^{-1}bar^{-1.66}\mu m^{3}$), and activation energy E_a=213.07 (kJ/mol) (Schmid et al., 1977). To
312 estimate the evolution or residual shear strength in our experiments (Figure 3), together with the
313 previous parameters for GBS, we used the measured velocity and temperature $T_{1.5}$. We considered
314 a thickness of the deforming zone h=100 μm and a grain size ϕ=8-16 nm and ϕ=40 nm for the
315 experiments performed at 6 m/s and 0.3 m/s, respectively. These values for h and ϕ are
316 compatible with those observed in microstructural studies performed on samples deformed under
317 similar loading conditions (Fig. S1, Spagnuolo et al., 2015; Violay et al., 2013). Our estimates of the
318 residual shear strength (Eq. 2) using the measured temperature are in agreement with the residual
319 shear strength measured at large displacement ($12 < d < 17$ m) in the experiments performed at
320 both low and high velocity (Figure 3a). At large displacement ($d > 5$ m), experiments at 0.3 m/s
321 display shortening, indicating extrusion of wear material from the shear surface and yield of the
322 wall rocks. The latter is favored by the longer duration of the experiment at 0.3 than at 6 m/s,
323 promoting heat diffusion and migration of the decarbonation reaction front from the shear
324 surface to the wall rocks. For Carrara marble rock, the slip weakening distance D_w has a power-law
325 dependence with normal stress ($D_w \approx a \cdot \sigma^{-b}$ with a = 160.17 $MPa^{1.3}$ and b = -1.3; Di Toro et al.,
326 2011). Therefore, the viscous creep deformation processes activated in our experiments at ca. 12-

17 m of slip, at seismogenic depths of ca. 10 km (normal stress ca. 250 MPa) can be activated after a slip distance of 0.15-0.10 m.

4.4 Implications for *on-fault* energy budget in simulated earthquakes

The temperature measurements in the sliding surface can be used to estimate the amount of frictional heat dissipated during simulated seismic slip and compare this value to the mechanical work *W* to shear the sample (Aubry et al., 2018; Lockner & Okubo, 1983). The total frictional work per unit area *W* (J/m^2) dissipated on the shearing surface is:

$$W = \int_0^{t_{fin}} \tau(t)V(t)dt \quad (3)$$

With τ the shear strength (Pa), *V* the velocity (m/s) both measured during the HVF experiments, and t_{fin} the total duration time of the experiment. Instead, the frictional heat per unit area *Q* (J/m^2) dissipated on the shearing surface can be measured independently as (Aubry et al., 2018):

$$Q = \rho(c_p T + L)\sqrt{\pi \alpha_{th} t} \quad (4)$$

With *T* temperature (K), *t* time (s), *L* latent heat (J/kg), ρ density (for calcite, 2860 kg/m^3), c_p the rock heat capacity, α_{th} the thermal diffusivity, defined as $\alpha_{th}=k/(\rho \cdot c_p)$, with *k* the thermal conductivity. The temperature-dependent heat capacity and thermal conductivity of Carrara marble (Merriman et al., 2018) are included in the calculation. For a first order comparison between the mechanical work and the heat dissipated we ignored the heat absorbed by the decarbonation reaction by setting the latent heat *L*=0. Because of this, our estimate of heat dissipation has to be considered an upper bound value (Figure 3b). In all the experiments, the total

heat is slightly higher than the total frictional work for the initial part of the experiment, and becomes lower than the total frictional work towards the end of the experiment (Figure 3b). This suggests that: i) at the beginning of the experiment, a heat sink related to thermal decomposition reaction should be subtracted from the calculated heat, and ii) towards the end of the experiments, part of the mechanical work was absorbed from other energy sinks, including decarbonation in the wall rocks of the shearing surface and cooling convection of the spinning sample in air. Whatever the case, these experiments with high resolution temperature measurements in the slip zone suggest that most of the seismic mechanical work is converted into heat and related-processes (decarbonation). Grain size reduction (down to the nano-scale) due to cataclasis and wear, if not directly related to the breakdown of the calcite lattice because of decarbonation, is a negligible energy sink. However, these experiments were performed on solid "pre-cut" specimens and therefore the energy dissipated by (i) fracture propagation and (ii) for strain localization during slip acceleration in gouge-built slip zones (Smith et al., 2015) is negligible.

5. Conclusions

We measured shear strength and temperature evolution during laboratory experiments replicating seismic slip in calcite-built rocks. Using the optical fiber, we measured the temperature in the slip zone with a sufficiently high spatial (ca. 37 μm) and temporal resolution (0.001 s) to provide insights into the mechanics of simulated seismic fault slip. A relevant result is that temperatures are of 1070-1250 °C when dynamic weakening is completed (Fig. 2), or 300-400°C higher than those previously measured with thermocouples and IR-cameras or modelled for similar experiments. Decarbonation of the marble could occur at these higher temperatures due to sustained high CO_2 pore pressure in the slip zone (0.8-4.5 MPa). Clearly, further studies are required to better constrain the contribution of decarbonation reaction to the heat sinks by, for

instance, introducing reaction kinetics depending on both temperature and CO_2 partial pressure. However, at the measured temperatures of 1070-1250 °C, the measured very low dynamic strength is compatible with the shear strength predicted by viscous creep processes. This implies that, in calcite-built rocks, fault strength during earthquake slip can be largely controlled by viscous creep processes. Lastly, by means of the *in-situ* real time high resolution temperature measurements, we infer that most of the mechanical work is largely dissipated as heat on the sliding surface.

References

Archard, J. F. (1959). The temperature of rubbing surfaces. *Wear*, *2*(6), 438–455. https://doi.org/10.1016/0043-1648(59)90159-0

Aretusini, S., Núñez-Cascajero, A., Spagnuolo, E., Tapetado, A., Vázquez, C., & Toro, G. Di. (2020). Mechanical data of rotary shear experiments and temperature measurements for the manuscript: "Fast and localized temperature measurements during simulated earthquakes in carbonate rocks" https://doi.org/10.5281/ZENODO.4288959

Ashby, M. F., & Verrall, R. A. (1973). Diffusion-Accommodated Flow and Superplasticity. *Acta Metallurgica*, *21*(2), 149–163. https://doi.org/10.1016/0001-6160(73)90057-6

Aubry, J., Passelègue, F. X., Deldicque, D., Girault, F., Marty, S., Lahfid, A., et al. (2018). Frictional Heating Processes and Energy Budget During Laboratory Earthquakes. *Geophysical Research Letters*, *45*(22), 12,274-12,282. https://doi.org/10.1029/2018GL079263

Barbery, M. R., Chester, F. M., & Chester, J. S. (2019). Temperature and stress distribution on flash heated contacts in granite at seismic slip rates. *AGUFM*, *2019*, MR42A-02. Retrieved from https://ui.adsabs.harvard.edu/abs/2019AGUFMMR42A..02B/abstract

Beeler, N. M., Tullis, T. E., & Goldsby, D. L. (2008). Constitutive relationships and physical basis of

396 fault strength due to flash heating. *Journal of Geophysical Research: Solid Earth*, *113*(1), 1–12.
397 https://doi.org/10.1029/2007JB004988
398 Chen, J., Yang, X., Yao, L., Ma, S., & Shimamoto, T. (2013). Frictional and transport properties of
399 the 2008 Wenchuan Earthquake fault zone: Implications for coseismic slip-weakening
400 mechanisms. *Tectonophysics*, *603*, 237–256. https://doi.org/10.1016/j.tecto.2013.05.035
401 Cornelio, C., Spagnuolo, E., Di Toro, G., Nielsen, S., & Violay, M. (2019). Mechanical behaviour of
402 fluid-lubricated faults. *Nature Communications*, *10*(1), 1–7. https://doi.org/10.1038/s41467-
403 019-09293-9
404 Criado, J. M., González, M., Málek, J., & Ortega, A. (1995). The effect of the CO2 pressure on the
405 thermal decomposition kinetics of calcium carbonate. *Thermochimica Acta*, *254*(C), 121–127.
406 https://doi.org/10.1016/0040-6031(94)01998-V
407 Demurtas, M., Fondriest, M., Balsamo, F., Clemenzi, L., Storti, F., Bistacchi, A., & Di Toro, G. (2016).
408 Structure of a normal seismogenic fault zone in carbonates: The Vado di Corno Fault, Campo
409 Imperatore, Central Apennines (Italy). *Journal of Structural Geology*, *90*, 185–206.
410 https://doi.org/10.1016/j.jsg.2016.08.004
411 Demurtas, M., Smith, S. A. F., Prior, D. J., Brenker, F. E., & Di Toro, G. (2019). Grain size sensitive
412 creep during simulated seismic slip in nanogranular fault gouges: constraints from
413 Transmission Kikuchi Diffraction (TKD). *Journal of Geophysical Research: Solid Earth*.
414 https://doi.org/10.1029/2019jb018071
415 Green, H. W., Shi, F., Bozhilov, K., Xia, G., & Reches, Z. (2015). Phase transformation and
416 nanometric flow cause extreme weakening during fault slip. *Nature Geoscience*, *8*(6), 448–
417 489. https://doi.org/10.1038/NGEO2436
418 Han, R., Shimamoto, T., Hirose, T., Ree, J. H., & Ando, J. I. (2007). Geophysics: Ultralow friction of
419 carbonate faults caused by thermal decomposition. *Science*, *316*(5826), 878–881.

https://doi.org/10.1126/science.1139763

Lockner, D. A., & Okubo, P. G. (1983). Measurements of frictional heating in granite. *Journal of Geophysical Research: Solid Earth*, *88*(B5), 4313–4320. https://doi.org/10.1029/JB088iB05p04313

McKenzie, D., & Brune, J. N. (1972). Melting on Fault Planes During Large Earthquakes. *Geophysical Journal International*, *29*(1), 65–78. https://doi.org/10.1111/j.1365-246X.1972.tb06152.x

Merriman, J. D., Hofmeister, A. M., Roy, D. J., & Whittington, A. G. (2018). Temperature-dependent thermal transport properties of carbonate minerals and rocks. *Geosphere*, *14*(4), 1961–1987. https://doi.org/10.1130/GES01581.1

Miao, S. Q., Li, H. P., & Chen, G. (2014). Temperature dependence of thermal diffusivity, specific heat capacity, and thermal conductivity for several types of rocks. *Journal of Thermal Analysis and Calorimetry*, *115*(2), 1057–1063. https://doi.org/10.1007/s10973-013-3427-2

Mitchell, T. M., Smith, S. A. F., Anders, M. H., Di Toro, G., Nielsen, S., Cavallo, A., & Beard, A. D. (2015). Catastrophic emplacement of giant landslides aided by thermal decomposition: Heart Mountain, Wyoming. *Earth and Planetary Science Letters*, *411*, 199–207. https://doi.org/10.1016/j.epsl.2014.10.051

Nielsen, S., Spagnuolo, E., & Violay, M. (2012). Composite sample mount assembly (SAMOA): The ultimate sample preparation for rotary shear experiments. *INGV Rapporti Tecnici*, 2039–741.

Nielsen, S., Spagnuolo, E., Violay, M., Smith, S. A. F., Di Toro, G., & Bistacchi, A. (2016). G: fracture energy, friction and dissipation in earthquakes. *Journal of Seismology*, *20*(4), 1187–1205. https://doi.org/10.1007/s10950-016-9560-1

Núñez-Cascajero, A., Tapetado, A., & Vazquez, C. (2020). High spatial resolution optical fiber two colour pyrometer with fast response. *IEEE Sensors Journal*, 1–1. Retrieved from

https://ieeexplore.ieee.org/document/9187346/

Ohl, M., Plümper, O., Chatzaras, V., Wallis, D., Vollmer, C., & Drury, M. (2020). Mechanisms of fault mirror formation and fault healing in carbonate rocks. *Earth and Planetary Science Letters*, *530*, 115886. https://doi.org/10.1016/j.epsl.2019.115886

Ohnaka, M., & Shen, L. (1999). Scaling of the shear rupture process from nucleation to dynamic propagation: Implications of geometric irregularity of the rupturing surfaces. *Journal of Geophysical Research: Solid Earth*, *104*(B1), 817–844. https://doi.org/10.1029/1998jb900007

De Paola, N., Hirose, T., Mitchell, T., Di Toro, G., Viti, C., & Shimamoto, T. (2011). Fault lubrication and earthquake propagation in thermally unstable rocks. *Geology*, *39*(1), 35–38. https://doi.org/10.1130/G31398.1

De Paola, N., Holdsworth, R. E., Viti, C., Collettini, C., & Bullock, R. (2015). Can grain size sensitive flow lubricate faults during the initial stages of earthquake propagation? *Earth and Planetary Science Letters*, *431*, 48–58. https://doi.org/10.1016/j.epsl.2015.09.002

Pozzi, G., De Paola, N., Nielsen, S., Holdsworth, R. E., & Bowen, L. (2018). A new interpretation for the nature and significance of mirror-like surfaces in experimental carbonate-hosted seismic faults. *Geology*, *46*(7), 583–586. https://doi.org/10.1130/G40197.1

Pozzi, G., De Paola, N., Holdsworth, R. E., Bowen, L., Nielsen, S., & Dempsey, E. D. (2019). Coseismic ultramylonites: An investigation of nanoscale viscous flow and fault weakening during seismic slip. *Earth and Planetary Science Letters*, *516*, 164–175. https://doi.org/10.1016/j.epsl.2019.03.042

Rempe, M., Di Toro, G., Mitchell, T. M., Smith, S. A. F., Hirose, T., & Renner, J. (2020). Influence of effective stress and pore-fluid pressure on fault strength and slip localization in carbonate slip zones. *Journal of Geophysical Research: Solid Earth*, *125*(11). https://doi.org/10.1029/2020jb019805

Rice, J. R. (2006). Heating and weakening of faults during earthquake slip. *Journal of Geophysical Research: Solid Earth*, *111*(5), 1–29. https://doi.org/10.1029/2005JB004006

Rodriguez-Navarro, C., Ruiz-Agudo, E., Luque, A., Rodriguez-Navarro, A. B., & Ortega-Huertas, M. (2009). Thermal decomposition of calcite: Mechanisms of formation and textural evolution of CaO nanocrystals. *American Mineralogist*, *94*(4), 578–593. https://doi.org/10.2138/am.2009.3021

Sarnes, B., & Schrüfer, E. (2007). *Determination of the time behaviour of thermocouples for sensor speedup and medium supervision*. *Proc. Estonian Acad. Sci. Eng* (Vol. 13).

Schmid, S. M., Boland, J. N., & Paterson, M. S. (1977). Superplastic flow in finegrained limestone. *Tectonophysics*, *43*(3–4), 257–291. https://doi.org/10.1016/0040-1951(77)90120-2

Schmid, S. M., Panozzo, R., & Bauer, S. (1987). Simple shear experiments on calcite rocks: rheology and microfabric. *Journal of Structural Geology*, *9*(5–6), 747–778. https://doi.org/10.1016/0191-8141(87)90157-X

Scholz, C. H. (2019). *The Mechanics of Earthquakes and Faulting*. *The Mechanics of Earthquakes and Faulting*. Cambridge University Press. https://doi.org/10.1017/9781316681473

Scholz, C. H., & Engelder, J. T. (1976). The role of asperity indentation and ploughing in rock friction -- I: Asperity creep and stick-slip. *International Journal of Rock Mechanics and Mining Sciences & Geomechanics*, *13*(5), 149–154. https://doi.org/10.1016/0148-9062(76)90820-2

Shimamoto, T., & Tsutsumi, A. (1994). A New Rotary-Shear High-Speed Frictional Testing Machine: Its Basic Design and Scope of Research. *Journal of Tectonic Research Group Japan*, *39*, 65–78.

Sibson, R. H. (1975). Generation of Pseudotachylyte by Ancient Seismic Faulting. *Geophysical Journal of the Royal Astronomical Society*, *43*(3), 775–794. https://doi.org/10.1111/j.1365-246X.1975.tb06195.x

Smith, S. A. F., Nielsen, S., & Di Toro, G. (2015). Strain localization and the onset of dynamic

492 weakening in calcite fault gouge. *Earth and Planetary Science Letters*, *413*, 25–36.
493 https://doi.org/10.1016/j.epsl.2014.12.043
494 Spagnuolo, E., Plümper, O., Violay, M., Cavallo, A., & Di Toro, G. (2015). Fast-moving dislocations
495 trigger flash weakening in carbonate-bearing faults during earthquakes. *Scientific Reports*, *5*,
496 1–11. https://doi.org/10.1038/srep16112
497 Sulem, J., & Famin, V. (2009). Thermal decomposition of carbonates in fault zones: Slip-weakening
498 and temperature-limiting effects. *Journal of Geophysical Research*, *114*(B3), B03309.
499 https://doi.org/10.1029/2008JB006004
500 Tapetado, A., Diaz-Alvarez, J., Miguelez, M. H., & Vazquez, C. (2016). Two-color pyrometer for
501 process temperature measurement during machining. *Journal of Lightwave Technology*,
502 *34*(4), 1380–1386. https://doi.org/10.1109/JLT.2015.2513158
503 Tapetado, A., Diaz-Alvarez, J., Miguelez, H., & Vazquez, C. (2017). Fiber-Optic Pyrometer for Very
504 Localized Temperature Measurements in a Turning Process. *IEEE Journal on Selected Topics in*
505 *Quantum Electronics*, *23*(2). https://doi.org/10.1109/JSTQE.2016.2627553
506 Tisato, N., Di Toro, G., De Rossi, N., Quaresimin, M., & Candela, T. (2012). Experimental
507 investigation of flash weakening in limestone. *Journal of Structural Geology*, *38*, 183–199.
508 https://doi.org/10.1016/j.jsg.2011.11.017
509 Di Toro, G., Niemeijer, A. R., Tripoli, A., Nielsen, S., Di Felice, F., Scarlato, P., et al. (2010). From
510 field geology to earthquake simulation: a new state-of-the-art tool to investigate rock friction
511 during the seismic cycle (SHIVA). *Rendiconti Lincei*, *21*(S1), 95–114.
512 https://doi.org/10.1007/s12210-010-0097-x
513 Di Toro, G., Han, R., Hirose, T., De Paola, N., Nielsen, S., Mizoguchi, K., et al. (2011). Fault
514 lubrication during earthquakes. *Nature*, *471*(7339), 494–498.
515 https://doi.org/10.1038/nature09838

516 Tsutsumi, A., & Shimamoto, T. (1997). High-velocity frictional properties of gabbro. *Geophysical*
517 *Research Letters*, *24*(6), 699–702. https://doi.org/10.1029/97GL00503
518 Usamentiaga, R., Venegas, P., Guerediaga, J., Vega, L., Molleda, J., & Bulnes, F. (2014). Infrared
519 Thermography for Temperature Measurement and Non-Destructive Testing. *Sensors*, *14*(7),
520 12305–12348. https://doi.org/10.3390/s140712305
521 Violay, M., Nielsen, S., Spagnuolo, E., Cinti, D., Di Toro, G., & Di Stefano, G. (2013). Pore fluid in
522 experimental calcite-bearing faults: Abrupt weakening and geochemical signature of co-
523 seismic processes. *Earth and Planetary Science Letters*, *361*, 74–84.
524 https://doi.org/10.1016/j.epsl.2012.11.021
525 Violay, M., Nielsen, S., Gibert, B., Spagnuolo, E., Cavallo, a., Azais, P., et al. (2014). Effect of water
526 on the frictional behavior of cohesive rocks during earthquakes. *Geology*, *42*(1), 27–30.
527 https://doi.org/10.1130/G34916.1
528 Violay, M., Di Toro, G., Nielsen, S., Spagnuolo, E., & Burg, J. P. (2015). Thermo-Mechanical
529 Pressurization of Experimental Faults in Cohesive Rocks during Seismic Slip. *Earth and*
530 *Planetary Science Letters*, *429*, 1–10. https://doi.org/10.1016/j.epsl.2015.07.054
531

532 References (Supplementary Information)

533 Cascajero, A. N., Tapetado, A., & Vazquez, C. (2020). High spatial resolution optical fiber two
534 colour pyrometer with fast response. *IEEE Sensors Journal*, 1–1.
535 https://doi.org/10.1109/JSEN.2020.3022179
536 Müller, B., & Renz, U. (2001). Development of a fast fiber-optic two-color pyrometer for the
537 temperature measurement of surfaces with varying emissivities. *Review of Scientific*
538 *Instruments*, 72(8), 3366–3374. https://doi.org/10.1063/1.1384448

539 Tapetado, A., Diaz-Alvarez, J., Miguelez, M. H., & Vazquez, C. (2016). Two-color pyrometer for
540 process temperature measurement during machining. *Journal of Lightwave Technology*,
541 34(4), 1380–1386. https://doi.org/10.1109/JLT.2015.2513158
542 Tapetado, A., Diaz-Alvarez, J., Miguelez, H., & Vazquez, C. (2017). Fiber-Optic Pyrometer for Very
543 Localized Temperature Measurements in a Turning Process. *IEEE Journal on Selected Topics*
544 *in Quantum Electronics*, 23(2). https://doi.org/10.1109/JSTQE.2016.2627553
545
546

547 Acknowledgements and Data

548 This work was supported by the ERC Consolidator grant 614705 NOFEAR and the Project MIUR
549 2020-2029 Working Earth – "Working Earth: geosciences and understanding of the earth dynamics
550 and natural hazards". This work was partially supported by grant RTI2018-094669-B-C32 SMART-
551 OF, Juan de la Cierva grant FJCI-2017-31677 and the Community of Madrid grant S2018/NMT-4326
552 SINFOTON2-CM.
553 S.A. thanks C. Cornelio, F. Passelegue, and S. Nielsen for insightful discussion about the
554 interpretation of the temperature measurements. The authors acknowledge the Editor, Kyu
555 Kanagawa and one anonymous reviewer for their constructive comments that helped to improve
556 the quality of the manuscript.
557 All data are available in a public repository (Aretusini et al., 2020).

Figure 1.

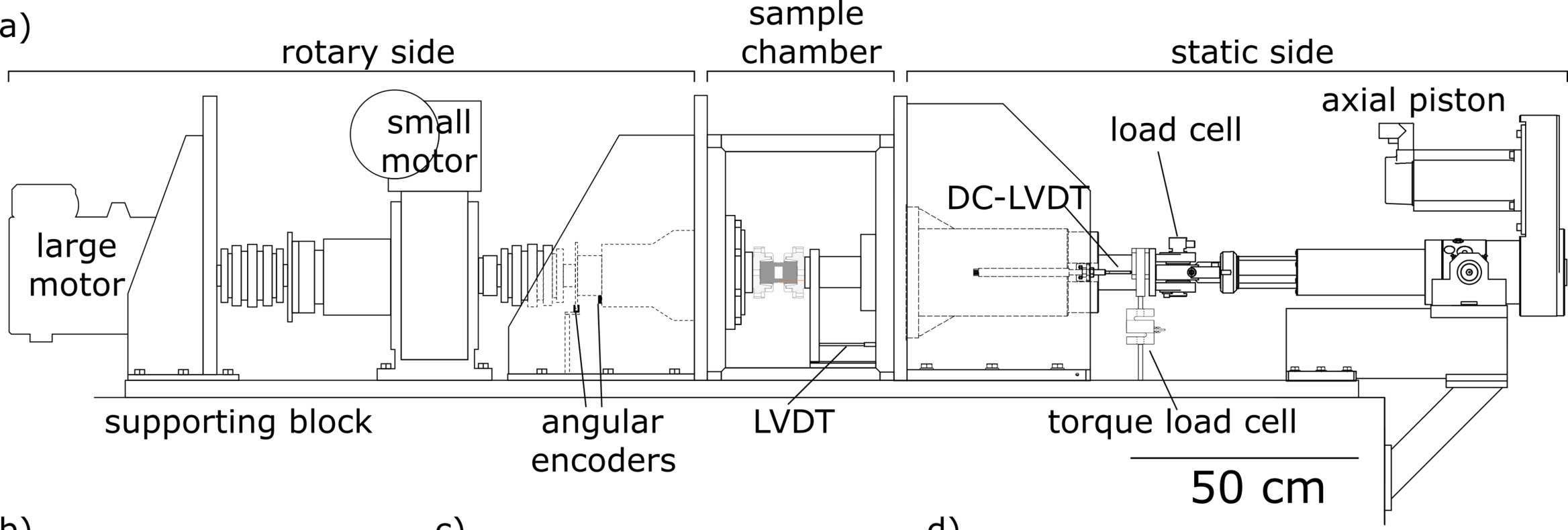
a)
rotary side
sample chamber
static side
small motor
large motor
axial piston
load cell
DC-LVDT
supporting block
angular encoders
LVDT
torque load cell
50 cm

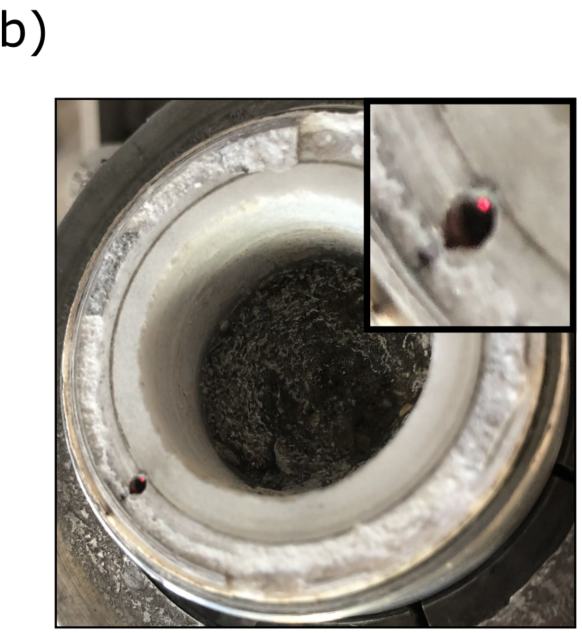
b)

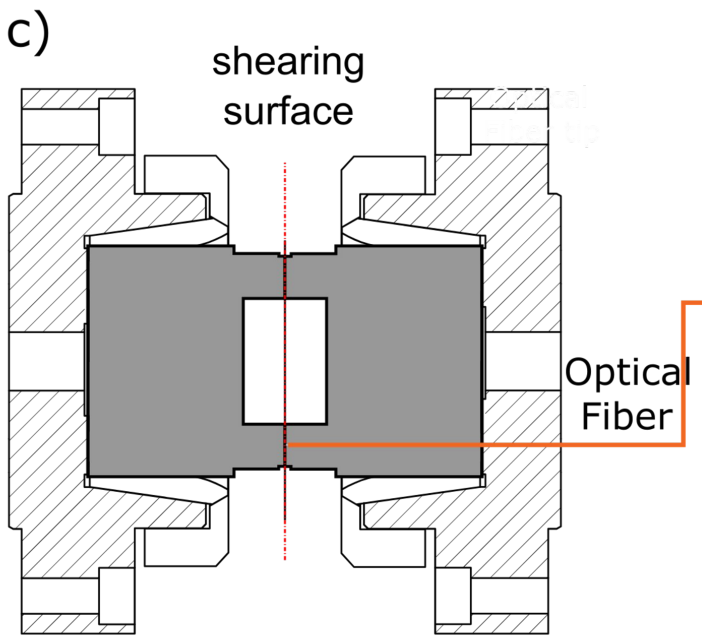
c)
shearing surface
Optical Fiber

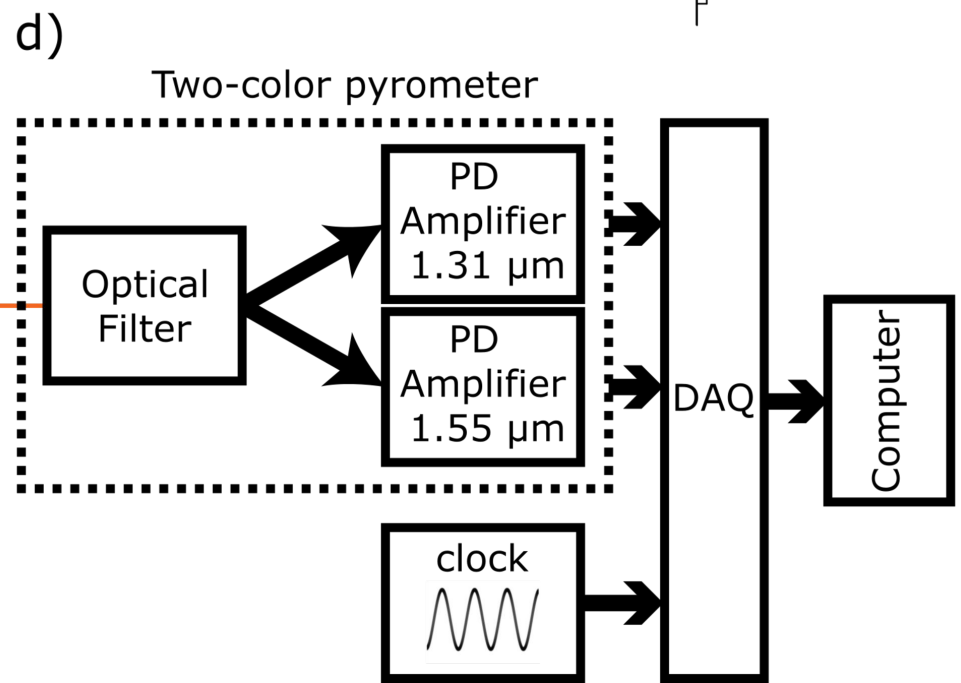
d)
Two-color pyrometer
Optical Filter
PD Amplifier 1.31 µm
PD Amplifier 1.55 µm
clock
DAQ
Computer

Figure 2.

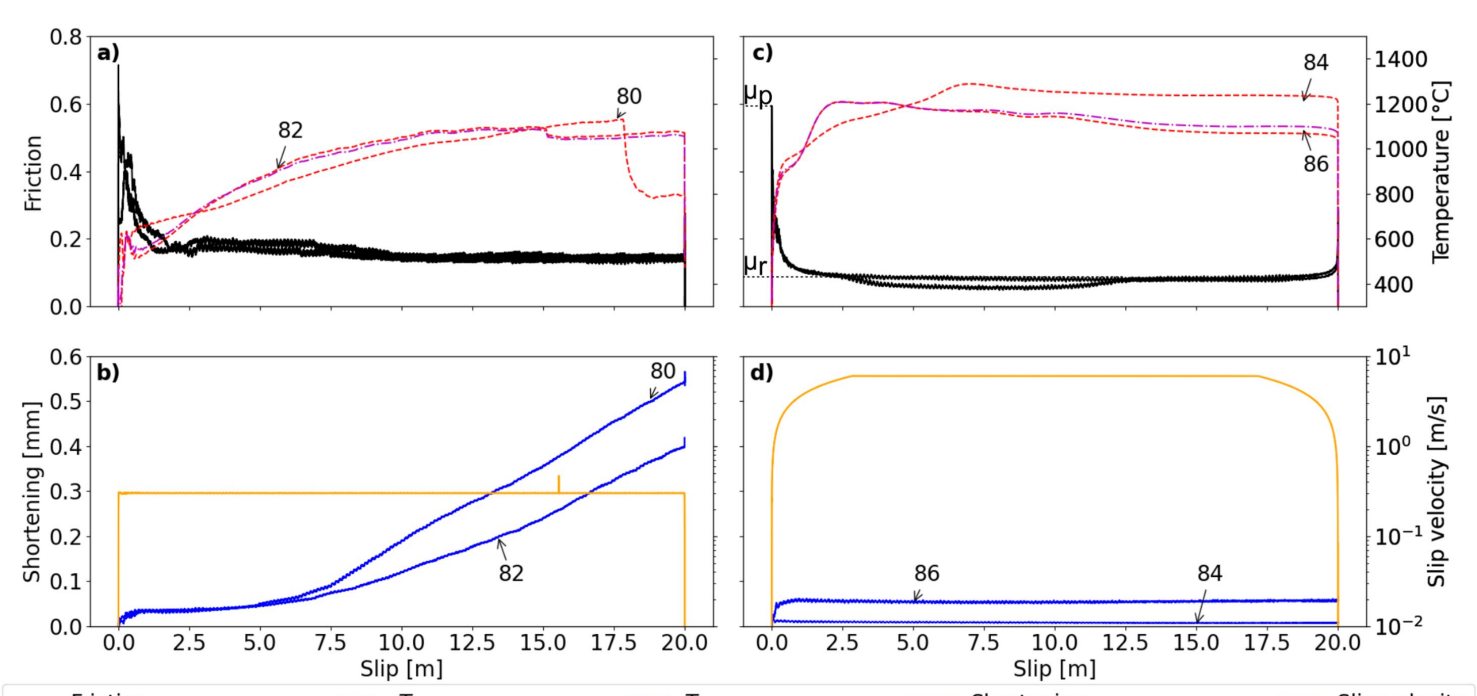
a)
Friction
82
80
c)
μp
μr
84
86
Temperature [°C]
b)
Shortening [mm]
80
82
Slip [m]
d)
86
84
Slip velocity [m/s]
Slip [m]
Friction
$T_{1.5}$
$T_{1.3}$
Shortening
Slip velocity

Figure 3.

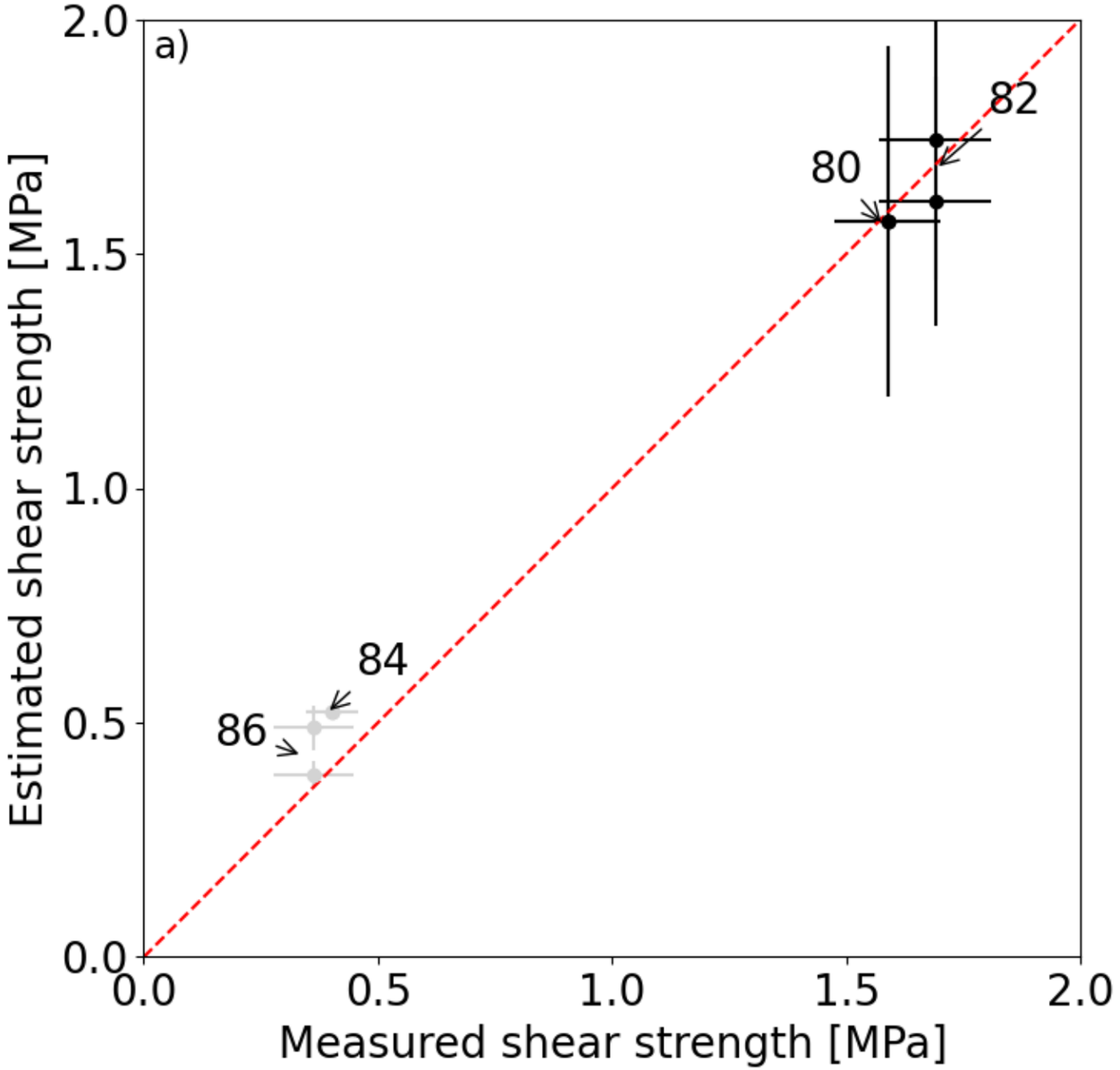
a)
2.0
1.5
1.0
0.5
0.0
Estimated shear strength [MPa]
0.0
0.5
1.0
1.5
2.0
Measured shear strength [MPa]
80
82
84
86

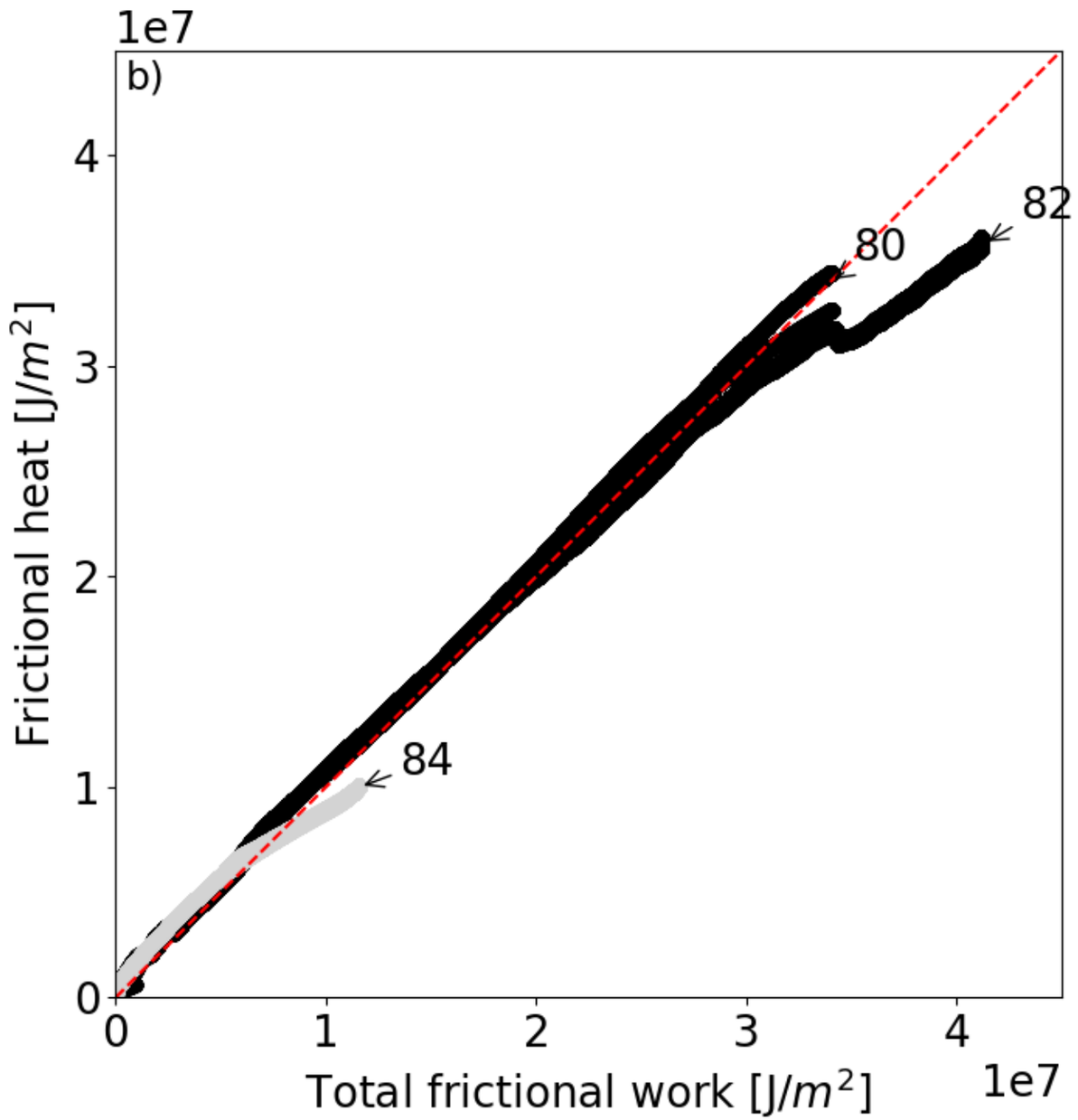
b)
1e7
4
3
2
1
0
Frictional heat [J/m²]
0
1
2
3
4
1e7
Total frictional work [J/m²]
80
82
84

V = 0.3 m/s V = 6 m/s